Experimental investigations and multi-objective optimization of an air-source absorption heat pump for residential district heating

Zhangxiang Wu [a, b], Shijun You [a, b], Huan Zhang [a, b], Yaran Wang [a, b *], Yan Jiang [a, b], Zhikai Liu [a, b], Li Sha [a], Shen Wei [c]

[a] School of Environmental Science and Engineering, Tianjin University, Tianjin, 300350, PR China

[b] Tianjin Key Lab of Biomass/Wastes Utilization, Tianjin 300350, PR China

[c] The Bartlett School of Construction and Project Management, University College London (UCL), 1-19 Torrington Place, London WC1E 7HB, United Kingdom

ABSTRACT: The traditional single-effect absorption heat pump is an effective district heating measure, while the low ambient temperature will degrade its performance significantly. To overcome this dilemma, a novel air-source absorption heat pump (ASAHP) for district heating (DH) is proposed in this paper. This system can operate at low ambient temperature and recover the waste heat of the flue gas with higher efficiency compared with the conventional gas-fired boilers. The falling film form is adopted in the generator and absorber, which reduces the system mass flow rate and electricity consumption. The thermodynamic performance of the system is analyzed by the lumped parameter model. An experimental rig is established to study the system performance and validate the mathematical model. Results show that the proposed system is an efficient way for DH, especially in cold regions. The heating capacity and the COP of the system are 38.32 kW and 1.39 at the evaporation temperature of -10 ℃, respectively. The system can provide 36.21 kW heating capacity and 39.21 kW heating capacity$_{fg}$ (heating capacity of the system

with flue gas recovery) with flue gas recovery to heat water from 25 ℃ to 39.1 ℃ with the COP of 1.21 and COP_{fg} (COP of the system with flue gas recovery) with flue gas recovery of 1.36. The maximum ratio of COP_{fg} with flue gas recovery to simulation value and the maximum ratio of heating $capacity_{fg}$ with flue gas recovery to simulation value are 92.91 % and 92.23 %, respectively. Additionally, to obtain the optimal operating condition, the TOPSIS decision-making method and NSGA-II technology is adopted in multi-objective optimization.

KEYWORDS: experiment study; mathematical model; absorption heat pump; system optimization

Nomenclature		**Subscript**	
c_p	constant pressure specific heat (kJ/kg·K)	abs	absorber
COP	coefficient of performance (unitless)	a	Air
Cl_i	proximity index (unitless)	c	cold
d_{i+}	the distance of any points to the ideal points (unitless)	cond	condenser
d_{i-}	the distance of any points to non-ideal points (unitless)	env	environment
ΔH_m	the heat of mixing of the R22-DEGDME (J/mol)	evap	evaporator
H	molar enthalpy (kcal/kg)	fg	flue gas recovery
h	specific enthalpy (kJ/kg)	gen	generator
J	heat equivalent of work (kg·m/kcal)	he	heat exchanger
m	mass flow rate (kg/s)	in	inlet
M	molecular weight (g/mol)	ng	natural gas
P	pressure (MPa)	out	outlet

Q	heat transfer rate (kW)	r	refrigerant
t	temperature (°C)	s	strong
T	temperature (K)	w	weak/water
W_P	power input (kW)		
Y	molar concentration (%)		
η_b	boiler efficiency (%)		

1. Introduction

In China, with the increase of population and development of urbanization, the building energy consumption increases rapidly, and it accounts for 24 % of the total social energy consumption [1]. District heating (DH) energy consumption accounts for about 20 % of total building energy consumption in cold regions [2]. The main DH technologies in China still rely on fossil fuels which have pollution and low efficiency-issues [3]. Renewable solutions and efficient heating technologies have been widely discussed, where the and air source heat pump is one of the most promising techniques with high utilization potential for DH [4].

The air source compression heat pump (ASCHP) and air source absorption heat pump (ASAHP) are two main techniques of air source heat pump. The ASCHP has been widely studied as it can absorb heat from the outdoor air and provide heat efficiently. Mahdi et al. [5] presented an ASCHP system and developed the thermodynamic and environment model to analyze the system performance. They concluded that the proposed system has good saving potentials for electricity and

natural gas with a payback period of 2.5 years. Yu et al. [6] proposed an ASCHP system and developed a mathematical model to assess the energy, economic and environmental performance of the heating system. They supposed that due to the advantages of energy conservation and environmental protection, the proposed heat pump system is suitable for space heating. Long et al. [7] have designed a solar-ASCHP system for heating and built a model to simulate the system. Results show that the system has a maximum COP of 2.68 and could operate with high efficiency for most of the heating period. Wu et al. [8] conducted an air source heat pump heating system integrated with a water storage tank which could improve the operating efficiency at low ambient temperature. They found that the average COP of the coldest day is 2.35, and the seasonal COP is 2.95. Although the COP of the electric heat pump (EHP) can reach and exceed 3 with good heating performance, it is driven by electric energy and the thermal efficiency of the power generation process has not been considered in the COP value [9].

Wu et al. [10] have indicated that the conventional ASCHP used in heating-dominated buildings have the problems of thermal imbalance and deterioration of heating performance. Zhang et al. [11] compared the EHP with the AHP on the same heat quantity condition and supposed that the AHP DH system has the advantage of lower first energy consumption. Under the same heating condition, the primary energy efficiency of the AHP DH system can be increased by about 42 % compared with the EHP. Anna et al. [12] compared the life cycle assessment results of EHP and AHP. They concluded that the AHP has lower environmental

effects than the EHP. Compared with ASCHP, ASAHP has the following advantages: high energy efficiency, environmental friendliness, and low cost. Therefore, many researchers have focused on the application and feasibility of the ASAHP. Christopher et al. [13] proposed a gas-fired single-effect ammonia-water AHP system for residential heating. They found that the AHP system could heat the water from 14.5 ℃ to 57.0 ℃ with the COP of 1.74 at the evaporation temperature of 20 ℃. The authors [14] have investigated an ASAHP system and recommended some optimal operating conditions. They concluded that the proposed system has better thermal performance compared with a conventional solar heating system with a COP of 1.72 at the evaporation temperature of 7 ℃. Garrabrant et al. [15] indicated the gas-fired AHP system could produce hot water of 45 ℃ with the COP of 1.63 under the same ambient temperature in Ref. [14]. Altamash et al. [16] studied a gas-fired AHP system and conducted that when the ambient temperature is -5 ℃, the primary energy efficiency is larger than 1. When the ambient temperature is lower than -5 ℃, the primary energy efficiency is less than 1. Dai et al. [17] designed a solar-driven ASAHP system and conducted the experimental and theoretical analysis of the system. They found that the COP can reach 1.44-1.66 when the ambient temperature is 4.32 ℃-11.07 ℃. The optimal generator temperature is 180 ℃ when the ambient temperature is 7 ℃ and the water outlet temperature is 45 ℃.

Hence, the ASAHP system has obvious advantages in the DH system. However, there are some limitations of the ASAHP for the application in cold regions with low ambient temperature. According to Ref. [18], the COP of the ASAHP system

decreases from 1.4 to 1.05 when the ambient temperature drops from 5.6 ℃ to -30 ℃. Besides, the working fluid of water-lithium bromide can not operate when the ambient temperature is less than 0 ℃ and the ammonia is flammable and toxic. To overcome these obstacles, innovations in working fluid and system structures are two main methods. At present, numerous researches have focused on the hybrid absorption-compression heat pump system to reduce the evaporation pressure and improve the absorption pressure [19,20]. However, such systems require a compressor, which results in system complexities and high initial costs. Another measure is to recovery the flue gas waste heat as conventional directly gas-fired and heating network based on gas boiler lack efficient method to conduct the flue gas waste heat recovery [21]. As the high-temperature flue gas contains a lot of water vapor with latent heat, it is necessary to recycle the waste heat of flue gas to improve the system performance [22]. However, the flue gas waste heat recovery relied on the backwater will result in incomplete heat utilization because the temperature of flue gas cannot be lower than the dew point. Qu et al. [23] designed an AHP system with a gas-liquid heat exchanger to recover the sensible and latent heat of the flue gas. They found that the energy efficiency will be increased by 10 % with the recovery of waste heat. Yang et al. [24] designed a full open AHP with total flue gas heat recovery used for DH. Experimental results display that the system COP can achieve 1.62 at the flue gas dew point of 36.2 ℃.

Additionally, the falling film heat exchanger is an efficient technology to improve the system form with a high heat transfer coefficient, less working fluid,

and small size [25]. However, most of the current literature mainly studies the flow and heat transfer of a single falling film heat exchange tube based on numerical and experimental methods. Compared with the single tube falling film, the process of falling film heat exchanger in the tube bundles is more easily affected by the steam direction and arrangement of the heat exchange tube with a complex heat transfer mechanism [26]. Besides the form improvement study of the ASAHP system, performance optimization considering efficiency is also a hot research topic that can optimize the variables to obtain the optimal operating conditions. Jain et al. [27] proposed an AHP system and analyzed its energy and exergy performance. They optimized the operating variables of the system according to the NSGA-II technology. The result shows that the optimal solution of the ASAHP is best outcome than any other single-objective optimized designs. The authors [28] designed a novel ASAHP with the flue gas recovery for DH. They conducted a multi-objective optimization method to search for the minimum payback period and exergy destruction of the system simultaneously. The optimized results concluded that the multi-objective optimization solutions show better performance than the single-objective optimization.

A review of these researches indicates that performance studies on the ASAHP system have been carried out by many researchers. However, there are four main limitations in the ASAHP system for heating. Firstly, existing systems can not operate with high efficiency in the cold region with conventional working fluid. Secondly, waste heat recovery of flue gas is not sufficient due to the lack of

low-temperature sources. Thirdly, the flow and heat transfer of a single heat exchange tube are always studied and there is a lack of knowledge on the falling film heat exchanger for absorber and generator. Fourth, there are few studies that apply multi-objective optimization in the ASAHP system to find the optimal operating conditions. Therefore, a novel air-source absorption heat pump (ASAHP) driven by the natural gas with R22-DEGDME as working fluid for DH is proposed and designed. The generator and absorber in this study have been designed as falling film heat exchangers to increase the heat transfer coefficient and reduce the mass flow rate. Then, a mathematical model is established to analyze the system performance, and an experiment rig based on the theoretical analysis is designed and set up. The system performance is investigated under different operating conditions of generator temperature, condensing temperature, and water flow rate. Additionally, the optimal operating conditions of the system can be obtained by the multi-objective optimization based on the TOPSIS decision-making method and NSGA-II technology.

2. System description

The schematic of the ASAHP system is shown in Fig. 1. The ASAHP consists of three loops which are working fluid loop in the black line, solution loop in the green and purple line, and hot water loop in the blue line. The working fluid loop includes a condenser, a reservoir, a heat exchanger-II, an electronic expansion valve (EEV), and an evaporator. The solution cycle consists of an absorber, a solution pump, a solution heat exchanger, a generator, and a controller. The main components

of the water loop are a water pump and a fan coil.

In the working fluid loop, the high temperature and pressure vapor is generated from the generator and goes to the condenser heating the hot water from the absorber. The liquid condensed in the condenser enters the reservoir and the heat exchanger-II. In the exchanger-II, the liquid working fluid temperature is lowered by the low temperature-pressure working fluid vapor. After passing the EEV, the pressure of the liquid drops to evaporation pressure. The low temperature and pressure working fluid absorbs heat from outdoor air and evaporates in the evaporator. Finally, the low temperature-pressure working fluid vapor absorbs heat in the exchanger-II and enters the absorber.

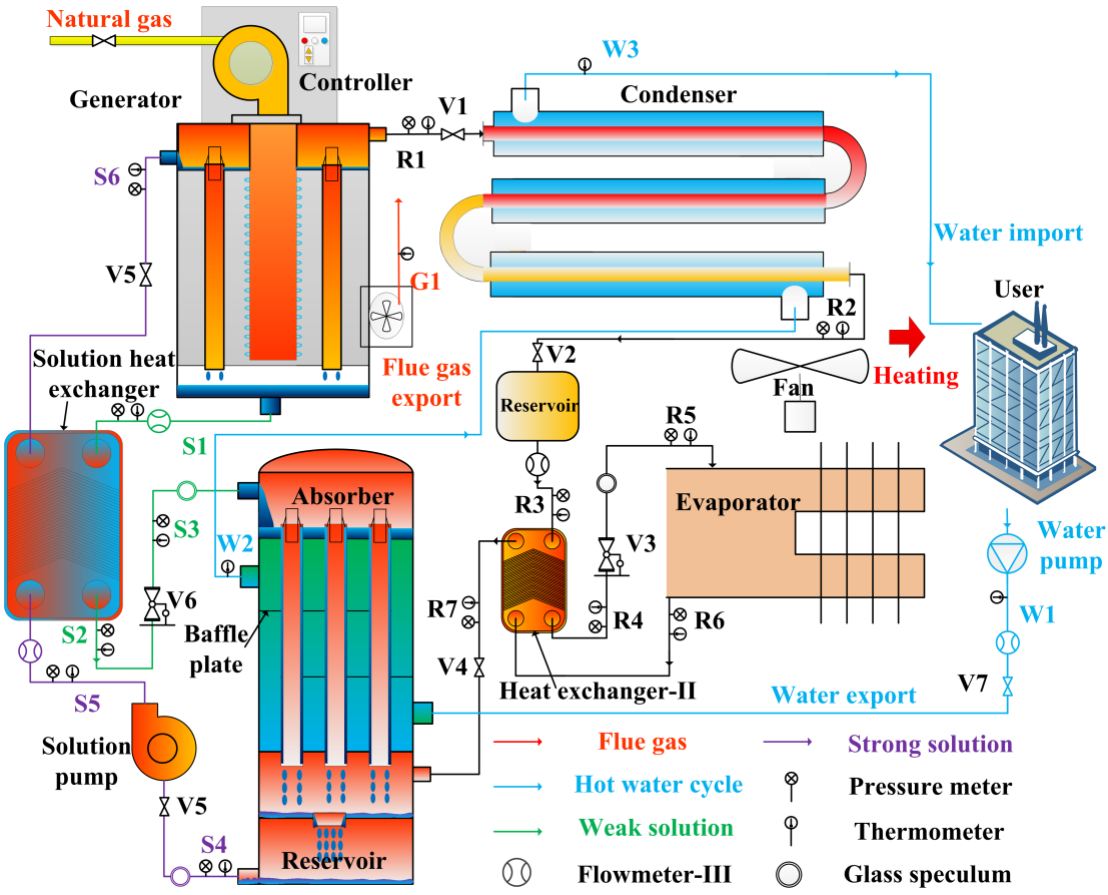

Fig. 1 Schematic view of the ASAHP system

The loop of the solution begins in the absorber. The weak solution absorbs the low pressure and temperature working fluid vapor and becomes a strong solution. The heat of solution and vapor mixing is transferred to the water. The strong solution from the reservoir can be pumped to the solution heat exchanger and absorbs heat from the weak solution. Then the high-pressure strong solution goes to the generator. In the generator, the combustor burns natural gas and releases heat to the strong solution. Then the strong solution changes to a weak solution and generates working fluid vapor. The working fluid vapor goes to the condenser and the weak solution enters the solution heat exchanger, releasing heat to the strong solution. After passing the EEV, the weak solution pressure drops to absorber pressure. Finally, the low-pressure weak solution returns to the absorber. The return water from the resident is heated by the absorber and condenser and finally supplied to the user.

Based on the previous simulation analysis and research, an experiment rig of the ASAHP system is established. Fig. 2 is a photo of the test bench of the system. The experimental rig is set up based on the schematic diagram shown in Fig. 1. Notably, the user in Fig. 1 is replaced by a fan coil used to free the heat. Before the system starts, the valves V1, V2, V4, and V5 are opened. The two electronic expansion valves V3 and V6 are controlled by two separate controllers.

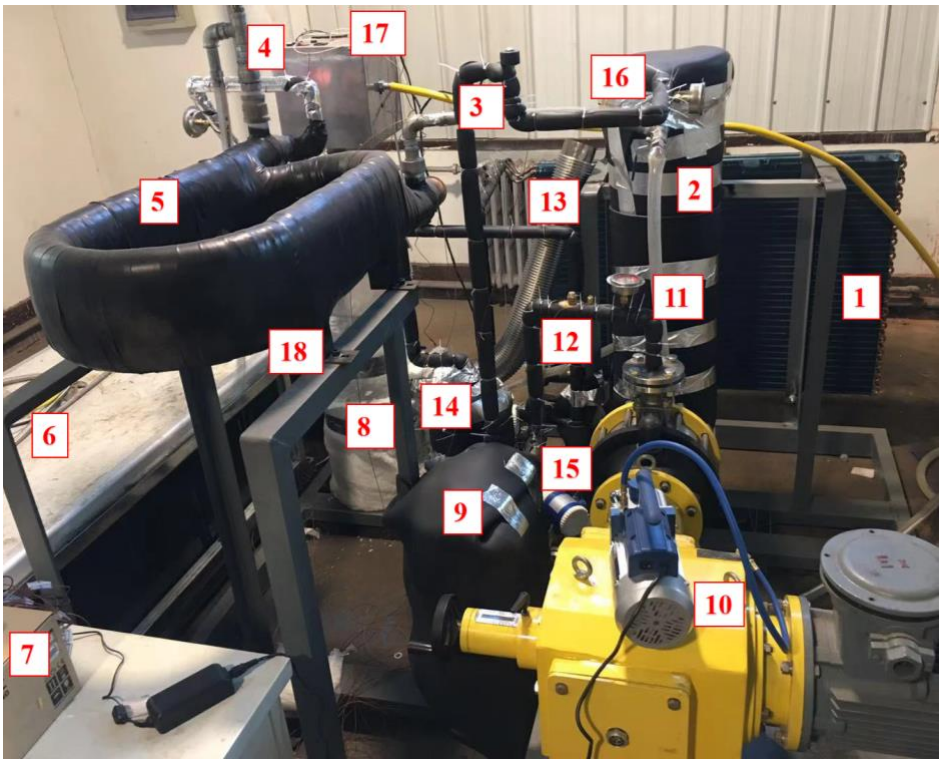

Fig. 2 Photo of the test bench

1-Evaporation, 2-Absorber, 3-EEV, 4-Combustor, 5-Condenser, 6-Fan coil, 7-Data acquisition machine, 8-Generator, 9-Solution heat exchanger, 10-Solution pump, 11-Pressure meter, 12-Valve, 13-Chimney, 14-Reservoir, 15-Volume flowmeter, 16-Glass speculum, 17-Controller, 18-Water flowmeter

The experimental system starts up in the following procedures. Firstly, opening the combustor by the controller to provide heat to the strong solution in the generator. Then, the solution pump is opened with a fixed volume to start the circulation of the solution. Finally, the fan coil and water pump are started to ensure that the water circulates. The suitable working fluid is important because it can reduce irreversible destruction and improve energy conversion efficiency. There have been many kinds of research on the absorption heat pump based on the water-lithium bromide and ammonia-water pairs. However, these two working pairs have some disadvantages.

The system with the working fluid of water-lithium bromide cannot be operated when the evaporation temperatures below 0 ℃, as water will freeze. The ammonia is flammable and toxic [29,30]. The hazards can be more obvious when the ammonia-water pairs are adopted as working fluid in gas-fired AHP. R22-DEGDME solution is nontoxic and nonflammable and can operate when the ambient temperature below 0 ℃ [28]. Although there have been some shortcomings in the environment with the ozone problem and global warming, this solution has good energy efficiency, application, and some useful knowledge [31]. It is worth noting that although the system with R22-DEGDME as a working fluid has good thermodynamic performance, it only provides some new guidance and direction for the selection of working fluid. R22-DEGDME won't be used in the future due to its high ODP and GWP according to the Kigali Amendment. Some properties of the solution have been displayed in Table 1.

Table 1 Some properties of the solution [28]

Parameters	R22	DEGDME
Molecular weight (g/mol)	86.46	134.17
Boiling point (℃) (P=0.101 MPa)	-40.8	162
Critical temperature (℃)	96.15	328.85
Density (kg/m^3) (t=20 ℃)	1210	944
Toxicity	No	No
Corrosivity	No	No

3. Methods

Fig. 3 shows the P-T diagram of the ASAHP system. The weak solution (S1) from the generator goes to the solution heat exchanger (S2). After the EEV (S3), it enters the absorber and absorbs working fluid vapor (R7). Then the weak solution (S1) becomes a strong solution (S4). After the pump (S5) and solution heat exchanger (S6), it goes to the generator. The working fluid vapor goes to the condenser (R1), reservoir (R2), heat exchanger-II (R3), EEV (R4), evaporator (R5), heat exchanger-II (R6) and enters absorber (R7). The mathematical model is established to analyze the system performance. The following assumptions are considered for simplification:

1) The system components work in a steady-state [10].
2) The solutions at the outlets of the generator and the absorber are saturated [28].
3) The working fluids are saturated at the outlets of the condenser and the evaporator [28].
4) The heat loss and pressure drop of all the equipment and pipes are neglected [9].

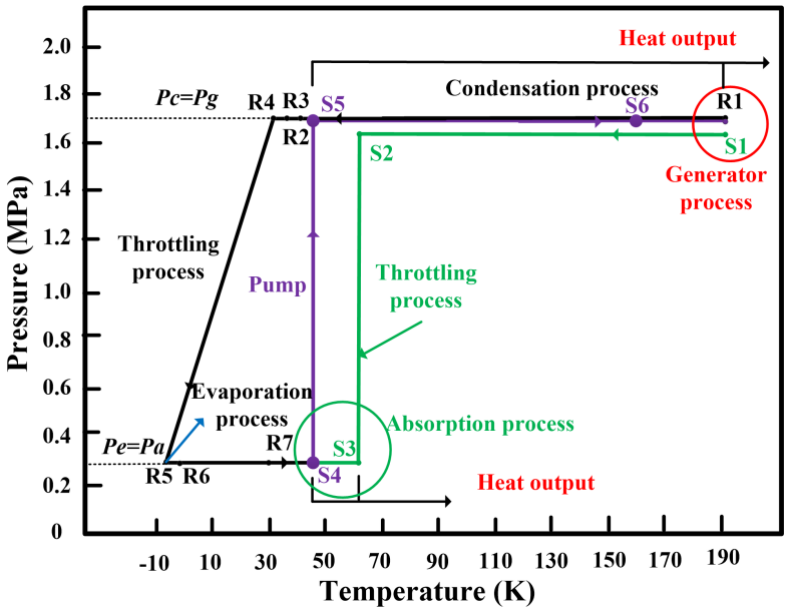

Fig. 3 P-T diagram of the ASAHP system

3.1. Model description

According to the Ref [28,32], there are three factors in the solution equilibrium equation which are the solution temperature *T*, R22 molar concentration *Y*, and the solution pressure *P*. The equation can be written as:

$$\ln P = \sum_{n=0}^{5} A_n Y^n + \frac{1}{T}\sum_{n=0}^{5} B_n Y^n + \ln T \cdot \sum_{n=0}^{5} C_n Y^n \tag{1}$$

The specific heat of the R22-DEGDME solution consisting of R22 molar concentration *Y* and the solution temperature *t* can be expressed as [28,32]:

$$c_p = \sum_{n=0}^{3} A_n^{c_p} Y^n + t\sum_{n=0}^{3} B_n^{c_p} Y^n + t^2 \cdot \sum_{n=0}^{3} C_n^{c_p} Y^n \tag{2}$$

The mixed heat of the solution can be defined as a function of R22 molar concentration *Y* [28,32].

$$\Delta H_m = Y(1-Y)\cdot \sum_{n=1}^{4} G_n (1-2Y)^{n-1} \tag{3}$$

The values of the constant coefficients A_n, B_n, C_n, $A_n^{c_p}$, $B_n^{c_p}$, $C_n^{c_p}$ and G_n in

Eqs.(1-3) are listed in Table A1 in Appendix A.

The solution molar enthalpy is defined as a function of specific heat c_p, mixed heat ΔH_m, R22 molar concentration Y, solution temperature t, heat equivalent of work J, molecular weights of DEGDME M_D and R22 M_{R22}. It can be formed as [28,32]:

$$H = \frac{\Delta H_m + \int_{10}^{t} c_p dt + \int_{0}^{10} c_p(Y=0)dt + Y\left(\int_{0}^{10} c_p(Y=1)dt - \int_{0}^{10} c_p(Y=0)dt\right)}{J(M_D(1-Y) + M_{R22}Y)} + 100 \tag{4}$$

Based on the first law of thermodynamic, the heat loads in the elements can be calculated. In the generator, the heat load depends on the weak solution, the strong solution, and the working fluid which can be defined as:

$$Q_{gen} = m_r \cdot h_{R1} + m_w \cdot h_{S1} - m_s \cdot h_{S6} \tag{5}$$

where m_r, m_w, and m_s are the mass flow rates of the working fluid, the weak solution, and the strong solution. h denotes the enthalpy of each state. As the generator is driven by natural gas combustion, the generator heat load Q_{gen} can also be calculated as:

$$Q_{gen} = q \cdot V_{ng} \tag{6}$$

where q is the calorific value and V_{ng} is the flow rate of the natural gas.

In the evaporator, heat is shifted from the outdoor air to the R22 and the amount of the heat is determined as:

$$Q_{eavp} = m_r(h_{R6} - h_{R5}) \tag{7}$$

In the condenser, water is heated by the working fluid vapor to the target temperature. In the absorber, water is heated by the mixed heat of working fluid and

weak solution. Therefore, the heating capacity includes two parts: condenser heat load and absorber heat load which can be calculated by:

$$Q_{cond} = m_r (h_{R2} - h_{R2}) = c_{p.w} \rho_w V_w (T_{W3} - T_{W2}) \tag{8}$$

$$Q_{abs} = m_r \cdot h_{R7} + m_w \cdot h_{S3} - m_s \cdot h_{S4} = c_{p.w} \rho_w V_w (T_{W2} - T_{W1}) \tag{9}$$

$$Q_{hc} = Q_{cond} + Q_{abs} = c_{p.w} \rho_w V_w (T_{W3} - T_{W1}) \tag{10}$$

In the solution heat exchanger and heat exchanger-II, the heat load can be written as:

$$Q_{she} = m_s (h_{S6} - h_{S5}) = m_w (h_{S1} - h_{S2}) \tag{11}$$

$$Q_{he-II} = m_r (h_{R4} - h_{R3}) = m_r (h_{R7} - h_{R6}) \tag{12}$$

The COP of the system is defined as:

$$COP = \frac{Q_{cond} + Q_{abs}}{Q_{gen} / \eta_b + W_p} \tag{13}$$

The mathematical model can be solved by following the calculation flow chart presented in Fig. 4.

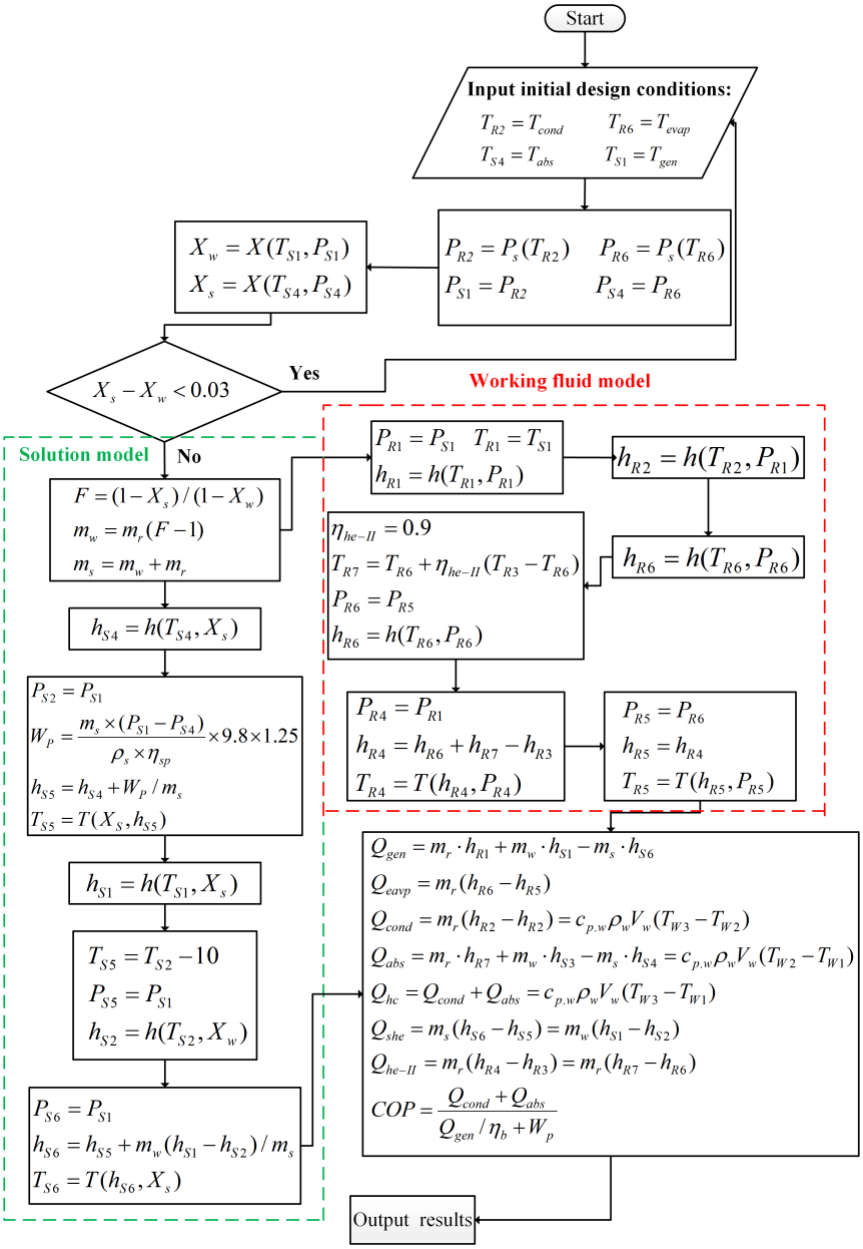

Fig. 4 The flow chart of system simulation

3.2. System multi-objective optimization

There is an opposition between the COP and supply water temperature with the increase of the water flow rate. A higher COP requires the supply water temperature to be lower, and a higher supply water temperature causes a lower COP. Therefore, system optimization with multi-objective should be examined in this study. Multi-objective optimization has been widely employed in the conflicting objectives

because this approach can provide an optimized result based on two objectives at the same time [33]. The COP and supply water temperature (T_{W3}) has been elected as the objective functions which can be described by the mathematical model in Section 3.1.

There are three optimization cases that take the COP as a single objective function, the supply water temperature as a single objective function, and both as a multi-objective function, respectively. The water flow rate and generator temperature are regarded as the decision variables, which are the principal factors that influence the COP and supply water temperature [27]. The equality constraints are formulated by the mathematical model. The inequality constraints are determined by the working conditions within safety ranges. The two decision variables of the proposed ASAHP are optimized by the NSGA-II technology, an effective technology to search for the optimal results [34]. Details of the NSGA-II technology with pseudo codes are referred from the appendix of Ref. [27]. In the optimization process, there is a Pareto frontier with many non-dominated solutions and each one of them is the ideal candidate [34]. Therefore, a final optimal solution should be selected from the Pareto frontier. TOPSIS method is adopted as it is a multi-criteria decision-making method and can yield the final optimal solution from the Pareto front [35]. Also, the Fuzzy method is used to conduct the non-dimensionalization of the COP and supply water temperature as follows: [37,38]

$$COP_i^n = \frac{\max(COP_i) - COP_i}{\max(COP_i) - \min(COP_i)} \tag{14}$$

$$T_{w.i}^{n} = \frac{\max(T_{w.i}) - T_{w.i}}{\max(T_{w.i}) - \min(T_{w.i})} \tag{15}$$

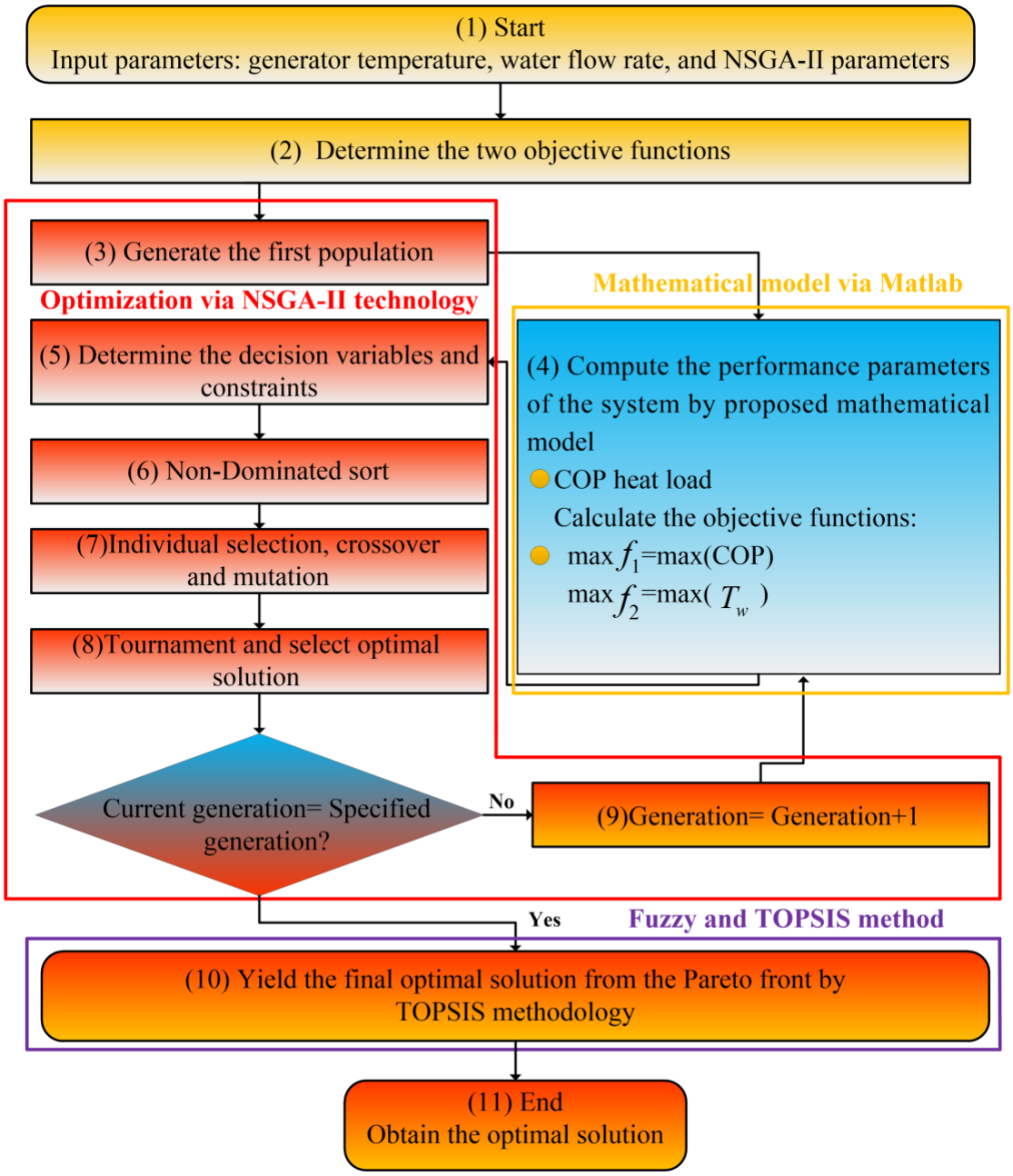

Fig. 5 Multi-objective optimization flowchart

According to the TOPSIS decision-making method, there are both ideal and non-ideal points. The ideal point can maximize the objective functions while the non-ideal point will minimize the objective functions. On the Pareto frontier, the

distance of any points to the ideal and non-ideal points are expressed as [39]:

$$d_{i+} = \sqrt{(COP_i - COP^{ideal})^2 + (T_{w.i} - T_w^{ideal})^2} \tag{16}$$

$$d_{i-} = \sqrt{(COP_i - COP^{non-ideal})^2 + (T_{w.i} - T_w^{non-ideal})^2} \tag{17}$$

The proximity index of the TOPSIS technology is defined by Eq.(18). If both the COP and supply water temperature are ideal points, Cl_i is 1; if they are non-ideal points, Cl_i will be 0 [40]. The maximum Cl_i will be decided as the optimal result and the optimization flow chart can be seen in Fig. 5.

$$Cl_i = \frac{d_{i-}}{d_{i-} + d_{i+}} \tag{18}$$

3.3. Experiment equipment and conditions

The experiment rig has been established according to the previous analysis and the main components of the system are listed in Table 2. Some detailed experiment operating conditions are presented in Table 3.

Table 2 Components of the system

Components	Type	Specification
Evaporator	DYGT-15	Finned tube exchanger. The heat transfer rate is 15 kW and the heat exchanger area is 28 m^2.
Condenser	TH-SCE25	Double-pipe exchangers. The heat transfer rate is 25 kW and the heat exchanger area is 12 m^2.
Electronic expansion valve	PCH-SD1N-002	The opening range is 0-500 step, the operating temperature is -30°C~70°C.
Solution pump	TL-D1800	Metering pump. The flow rate is 1.74 m^3/h, the voltage is 380 V, the pump heat is 158 m, and the rotary speed is 1450 rpm.
Fan coil	BFP-70WD	Ceiling air conditioning unit. The rated air volume is 7000 m^3/h and the cooling capacity is 50 kW.
Water pump	LRS-9	The flow rate is from 0 to7.8 m^3/h, the voltage is 220 V, the pump heat is 9 m, and the rotary speed is 3000 rpm

Flowmeter	YH-LWGYJD	Operating temperature is 60 ℃, the flow rate is from 0 to 6.62m^3/h
Solution heat exchanger	PL95-86	The heat transfer rate is 130 kW and the heat exchanger area is 10 m^2.
Heat exchanger-II	PL26-20	The heat transfer rate is 3 kW and the heat exchanger area is 1.5 m^2.
Thermometer	PT-100	-
Pressure meter	RL-2088	The pressure is from -0.1 to 60 MPa
Generator	-	Falling film heat exchanger. The heat transfer rate is 24 kW and the heat exchanger area is 0.36 m^2.
Absorber	-	Falling film heat exchanger. The heat transfer rate is 15 kW and the heat exchanger area is 1.2 m^2.
Data acquisition machine	GRAPHTEC-GL840	-

Table 3 Operating conditions of the system

Parameters	Range
Evaporating temperature	-10 ℃ - 0 ℃
Condensing temperature	40 ℃ - 45 ℃
Generator temperature	150 ℃ - 190 ℃
Water flow rate	1.5 m³/h - 2.4 m³/h
Volume of the solution pump	70 % - 100 %

3.4. Uncertainty analysis

The temperatures, flow rates, and pressures in Figs. 1 and 2 are all measured. In the experiment, a data acquisition instrument is approved to record the operating data for further analysis. In this subsection, uncertainty analysis is conducted to evaluate the test data. When the temperature, flow rate, and pressure are measured, there are two parts of uncertainty which are the random uncertainty and system uncertainty [21]. The total uncertainty can be calculated as:

$$\sigma_T = \sigma_R + \sigma_s \tag{19}$$

Based on the uncertainty analysis theory, for n measured parameters, the total

uncertainty can be determined by the related directly-measured parameters [21]. If y is a function of x_1, x_2, ..., x_n:

$$y = f(x_1, x_2, ..., x_n) \tag{20}$$

The total uncertainty of the function y can be defined as:

$$\sigma_T = \sqrt{(\frac{\partial f}{\partial x_1}\sigma_{T,x_1})^2 + (\frac{\partial f}{\partial x_2}\sigma_{T,x_2})^2 + \cdots + (\frac{\partial f}{\partial x_n}\sigma_{T,x_n})^2} \tag{21}$$

Taking the heat load as an example, the total uncertainty can be calculated as follows:

$$Q = c_{p.w}\rho V(T_1 - T_2) \tag{22}$$

$$\begin{aligned}\sigma_T &= \sqrt{(\frac{\partial f}{\partial V}\sigma_{T,V})^2 + (\frac{\partial f}{\partial T_1}\sigma_{T,T_1})^2 + (\frac{\partial f}{\partial T_2}\sigma_{T,T_2})^2} \\ &= c_{p.w}\rho\sqrt{(T_1 - T_2)^2\sigma_{T,V} + V^2(\sigma_{T,T_1}^2 + \sigma_{T,T_2}^2)}\end{aligned} \tag{23}$$

4. Results and discussions

4.1. System performance analysis

Table 4 shows the experimental parameters and the uncertainty of the ASAHP at a typical operating condition. According to the system described in Section 2, there is no flue gas waste heat recovery in the system which will lead to the reduction of COP. It is indicated in Ref. [28] that the available flue gas waste heat for each 24 kW natural gas combustion is about 3 kW. Therefore, a correction of 3 kW is added to the system heating capacity which will affect the heating capacity and COP. As listed in Table 4, the evaporation temperature is -9.1 ℃, the generator temperature is 189.7 ℃ and the supply water temperature is 39.7 ℃. The return water temperature is 25.5 ℃ and increases to 31.8 ℃ after passing the absorber with

a flow rate of 2.44 m³/h. According to the measured parameters, the heat load of each component can be calculated. It is shown from Table 5 that the system COP is 1.41. The energy input which consists of the evaporator load and the generator load is 36.81 kW, while the energy output including the condenser load and absorber load is 39.34 kW.

Table 4 Some experiment parameters and the uncertainty

Parameters	State point	Average value	System uncertainty
Temperature of weak in generator outlet	S1	189.7 ℃	±0.1 ℃
Temperature of weak in solution heat exchanger outlet	S2	55.8 ℃	±0.1 ℃
Temperature of weak solution in absorber inlet	S3	51.6 ℃	±0.1 ℃
Temperature of strong solution in absorber outlet	S4	43.3 ℃	±0.1 ℃
Temperature of strong solution in solution pump outlet	S5	44.2 ℃	±0.1 ℃
Temperature of strong solution in generator inlet	S6	152.1 ℃	±0.1 ℃
Temperature of working fluid in generator outlet	R1	185.5 ℃	±0.1 ℃
Temperature of working fluid in condenser outlet	R2	46.2 ℃	±0.1 ℃
Temperature of working fluid in reservoir outlet	R3	45.6 ℃	±0.1 ℃
Temperature of working fluid in heat exchanger-II outlet	R4	30.3 ℃	±0.1 ℃
Temperature of working fluid in evaportor inlet	R5	-9.1 ℃	±0.1 ℃
Temperature of working fluid in evaportor outlet	R6	2.6 ℃	±0.1 ℃
Temperature of working fluid in absorber inlet	R7	31.2 ℃	±0.1 ℃
Temperature of water in absorber inlet	W1	25.5 ℃	±0.1 ℃
Temperature of water in condenser inlet	W2	31.8 ℃	±0.1 ℃
Temperature of supply water	W3	39.7 ℃	±0.1 ℃

Water flow rate	Flowmater-IV	2.3 m³/h	±0.2 m³/h
Working fluid flow rate	Flowmater-III	0.25 m³/h	±0.02 m³/h
Strong solution flow rate	Flowmater-II	1.71 m³/h	±0.02 m³/h
Weak solution flow rate	Flowmater-I	1.38 m³/h	±0.02 m³/h
Natural gas flow rate	Controller	2.42 m³/h	±0.02 m³/h
Generator pressure	-	1.85 MPa	±0.01 MPa
Evaporation pressure	-	0.38 MPa	±0.01 MPa

Table 5 Performance analysis of typical condition

Equipment	Value	Accuracy
Evaporator load	12.99 kW	±0.42 kW
Generator load	23.91 kW	±0.38 kW
Absorber load	17.53 kW	±0.42 kW
Condenser load	18.81 kW	±0.48 kW
Solution pump	4 kW	-
COP	1.41	±0.05
Heating capacity	39.34 kW	±0.71 kW

Fig. 6 displays the variations of the tested and simulated COP with the increase of generator temperature under different evaporation temperatures. COP_{fg} is the COP after recovery of waste heat of flue gas. From Fig. 6(a), it can be observed that the tested COP, COP_{fg}, and simulated COP increase with the increase of generator temperatures at the evaporation temperature of -5 ℃. While the generator temperature reaches 190 ℃, the simulated COP is 1.71, COP_{fg} is 1.61 while the tested COP is 1.45. The ratio of tested COP and COP_{fg} to simulated COP increase and reach 85.04 % and 94.54% at the generator temperature of 190 ℃. Fig. 6(b), shows the variation of tested and simulated heating capacity with the increase of generator temperatures. $Heating\ capacity_{fg}$ is the heating capacity after recovery of

waste heat of flue gas. When the generator temperature reaches 190 ℃, the simulated heating capacity is 47.23 kW and heating capacity$_{fg}$ is 43.32 kW while the tested heating capacity is 40.32 kW. The ratio of tested heating capacity and heating capacity$_{fg}$ to simulated heating capacity increase with the increasing generator temperature and reach 85.37 % and 92.15 % at the generator temperature of 190 ℃.

Figs. 6(c) and 6(d) show the variation of heating capacity and COP with the increasing generator temperature at the evaporation temperature of -10 ℃. They show the same trend as when the evaporation temperature is -5 ℃. At the generator temperature of 190 ℃, the tested COP is 1.39 and the COP$_{fg}$ is 1.53 while the simulated COP is 1.65. The simulated heating capacity, heating capacity$_{fg}$, and tested heating capacity are 45.02 kW, 41.52 kW, and 38.32 kW, respectively. It can be explained by that the increase of generator temperature will result in the decrease of weak solution concentration and increase of refrigerant condenser inlet temperature; with unchanged strong solution concentration, the deflation ratio increases which leads to the rising absorption ability. The increasing absorption ability will lead to the increase of the mass flow rate of refrigerant. Further, the mass flow rate and the enthalpy difference of working fluid in the condenser rise leading to an increasing COP and heating capacity. Additionally, a higher evaporation temperature causes a higher evaporation pressure which leads to a higher absorber pressure. This will result in an increase in the deflation ratio with more heating capacity. Therefore, a higher generator temperature and higher evaporation temperature will cause a higher COP and heating capacity.

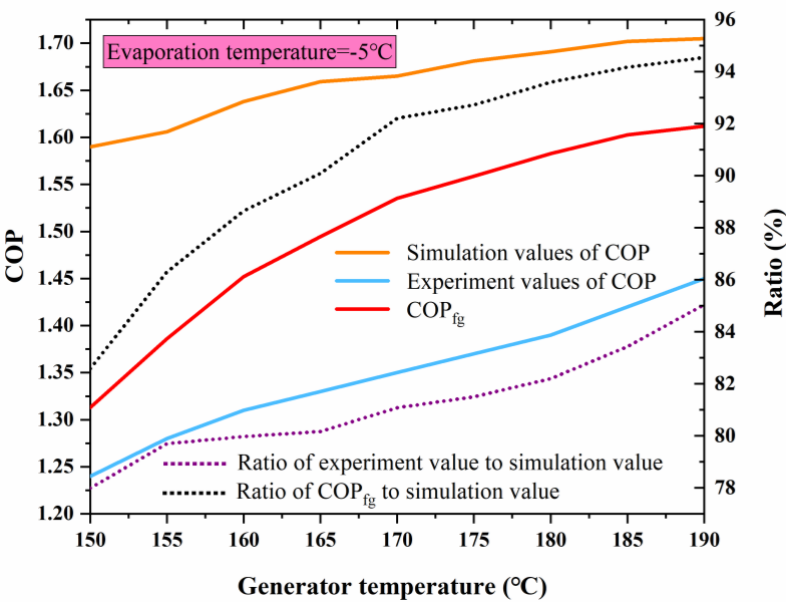
Evaporation temperature=-5℃
COP
Ratio (%)
Generator temperature (℃)
Simulation values of COP
Experiment values of COP
COP$_{fg}$
Ratio of experiment value to simulation value
Ratio of COP$_{fg}$ to simulation value

(a)

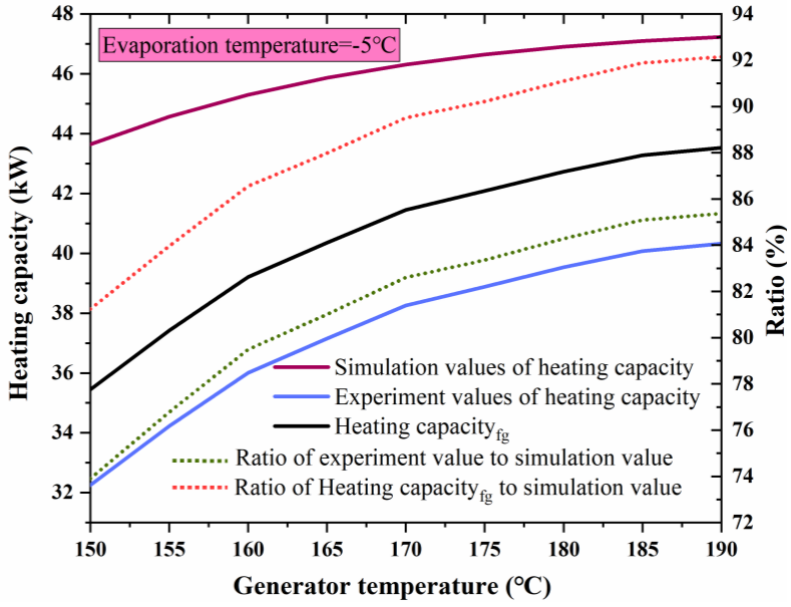
Evaporation temperature=-5℃
Heating capacity (kW)
Ratio (%)
Generator temperature (℃)
Simulation values of heating capacity
Experiment values of heating capacity
Heating capacity$_{fg}$
Ratio of experiment value to simulation value
Ratio of Heating capacity$_{fg}$ to simulation value

(b)

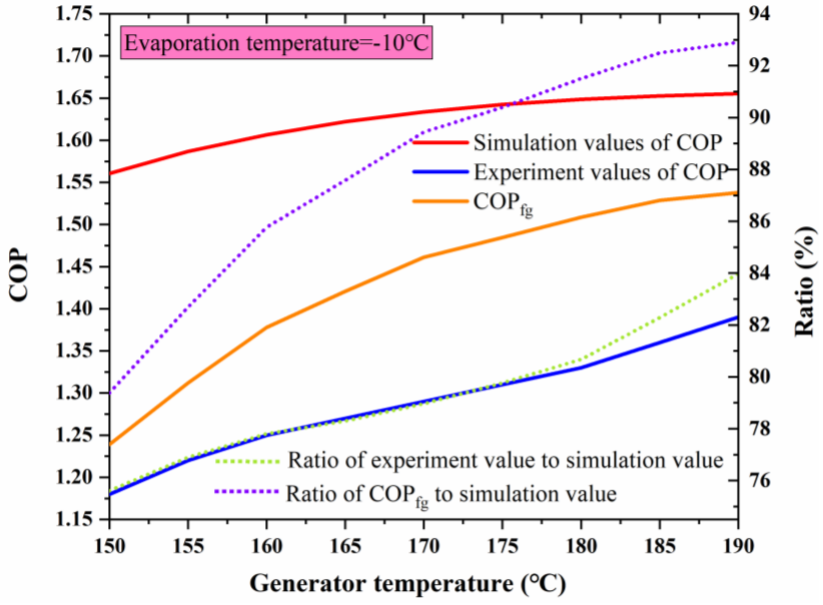

(c)

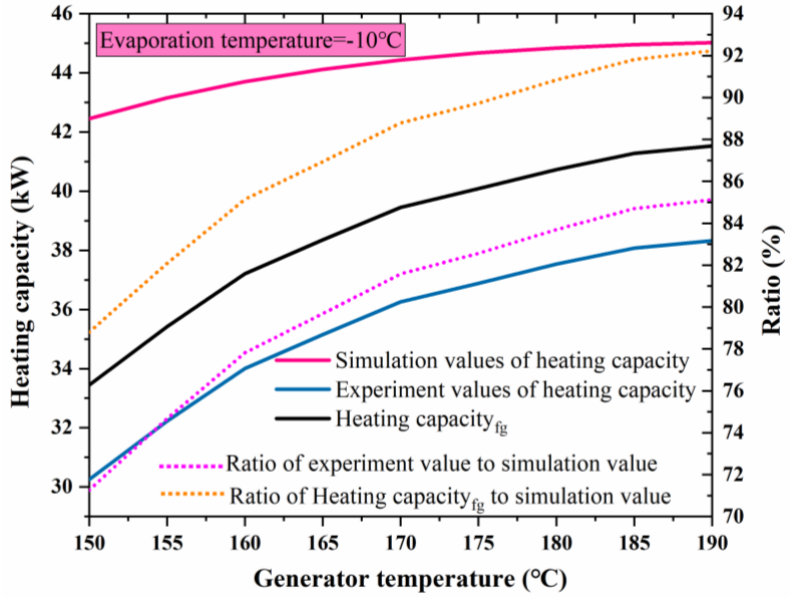

(d)

Fig. 6 Variation of COP and heating capacity under different generator and evaporation temperature

Fig. 7 illustrates the variation of COP under different condensing and evaporation temperatures. From the Figs. 7(a) and 7(c), the simulation COP, COP$_{fg,}$ and experiment COP decrease with the increasing supply water temperature under

the various evaporation temperatures. While the supply water temperature is 39 ℃, the COP reaches minimum value; the simulation COP is 1.61, COP_{fg} is 1.37 and experiment COP is 1.24 at the evaporation temperature of -5 ℃; the simulation COP is 1.57, COP_{fg} is 1.36 and experiment COP is 1.21 at the evaporation temperature of -10 ℃. At the evaporation temperature of -5 ℃, the ratio of experiment COP and COP_{fg} to simulation COP decrease and reach 85.04 % and 93.67 % when the supply water temperature is 30 ℃. At the evaporation temperature of -10 ℃, the ratio of experiment COP and COP_{fg} to simulation COP decrease and reach 81.55 % and 90.48 % at the supply water temperature of 30 ℃. Figs. 7(b) and 7(d) illustrate the change of heating capacity with the growing supply water temperature with the same trend of COP. When the supply water temperature is 39 ℃, the heating capacity is minimum; the simulation heating capacity is 46.18 kW, heating $capacity_{fg}$ is 39.61 kW and experiment heating capacity is 36.81 kW at the evaporation temperature of -5 ℃; the simulation heating capacity is 44.09 kW, heating $capacity_{fg}$ is 39.35 kW and experiment heating capacity is 36.55 kW at the evaporation temperature of -10 ℃. At the evaporation temperature of -5 ℃, the ratio of experiment heating capacity and heating $capacity_{fg}$ to simulation heating capacity drop and reach 85.37 % and 91.32 % at the supply water temperature of 30 ℃; while at the evaporation temperature of -10 ℃, the ratio of experiment heating capacity and heating $capacity_{fg}$ to simulation heating capacity decrease and reach 85.12 % and 91.33 % at the supply water temperature of 30 ℃. This is because that a higher supply water temperature results in a higher condensing temperature and pressure.

The improvement of condensing temperature causes the growth of working fluid enthalpy in the condenser outlet while the increase of condensing pressure will lead to the increase of weak solution concentration resulting in the reduction of the deflation ratio. These aspects will cause a decrease of mass flow rate of refrigerant and enthalpy difference in condenser leading to decreasing heating capacity and COP. Therefore, a lower supply water temperature will lead to enhanced heating capacity and COP.

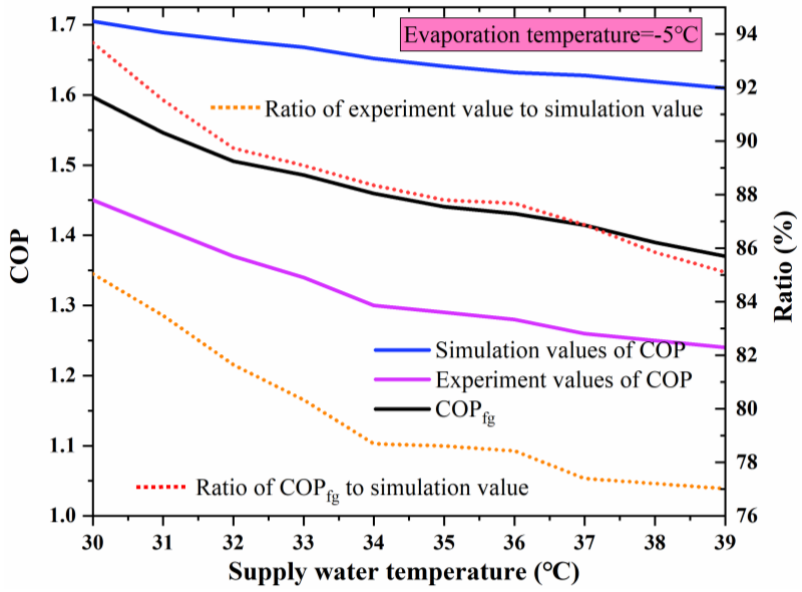

(a)

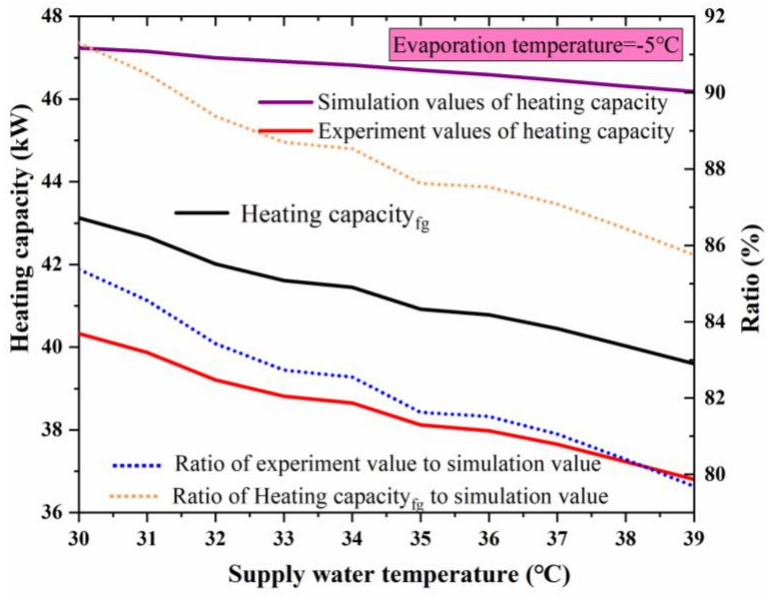
Evaporation temperature=-5℃
Simulation values of heating capacity
Experiment values of heating capacity
Heating capacity$_{fg}$
Ratio of experiment value to simulation value
Ratio of Heating capacity$_{fg}$ to simulation value
Heating capacity (kW)
Ratio (%)
Supply water temperature (℃)

(b)

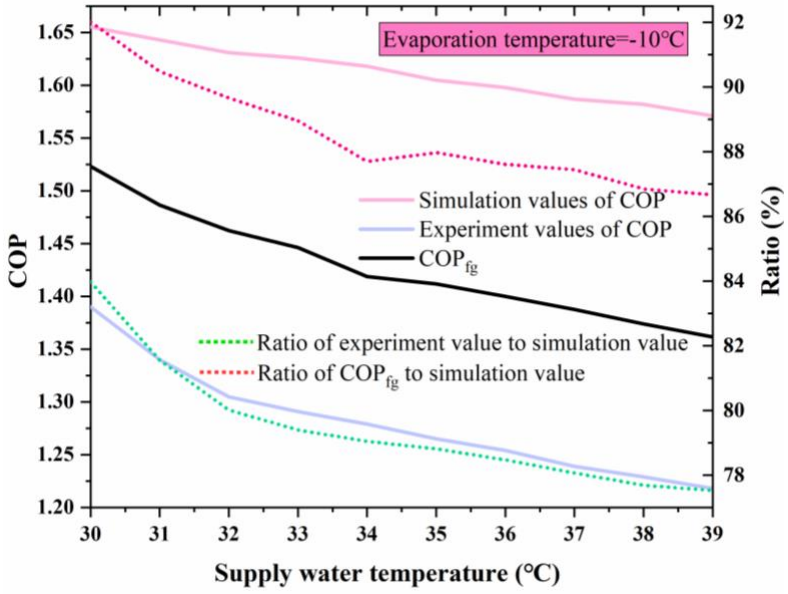
Evaporation temperature=-10℃
Simulation values of COP
Experiment values of COP
COP$_{fg}$
Ratio of experiment value to simulation value
Ratio of COP$_{fg}$ to simulation value
COP
Ratio (%)
Supply water temperature (℃)

(c)

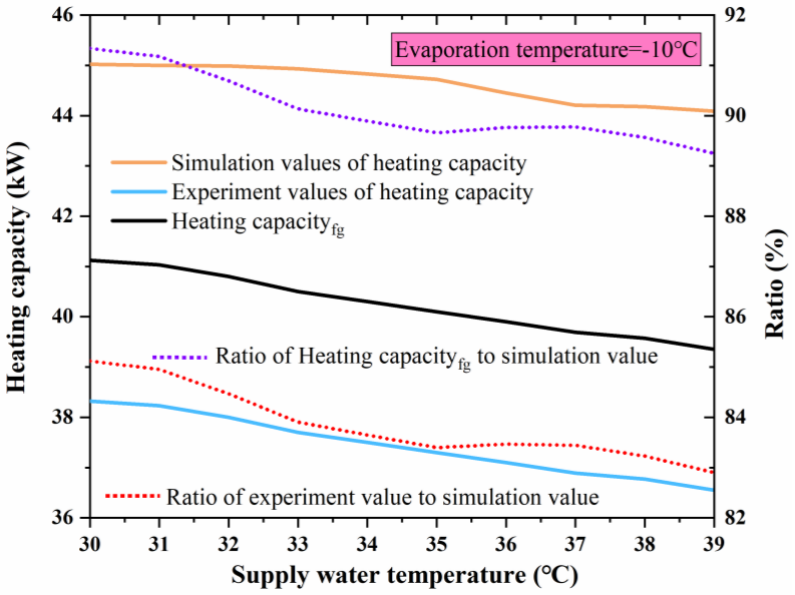

(d)

Fig. 7 Variation of COP and heating capacity under different condensing and evaporation temperature

Fig. 8 illustrates the heat load of each component under different evaporation temperatures. The heat load of the generator is similar in the simulation and experiment value in different evaporation values. This is because, in the experiment, the heat load of the generator is determined according to the flow rate of natural gas. Natural gas flow is controlled at about 2.4 m³/h that can produce about 24 kW of heat. As can be seen from Fig. 8, the simulation value is higher than the experimental value. This can be explained that there are heat loss and pressure loss during the experiment process. Besides, the heat of high-temperature flue gas is not fully utilized, resulting in the waste of heat. System efficiency will develop gently before the dew point of flue gas and begin to rise significantly after the dew point of flue gas. In this system, hot water can be heated by the flue gas to reduce the temperature

of the flue gas. Also, the evaporation temperature is far lower than the flue gas temperature, and the working fluid vapor at the evaporator outlet can be heated by the waste heat of flue gas.

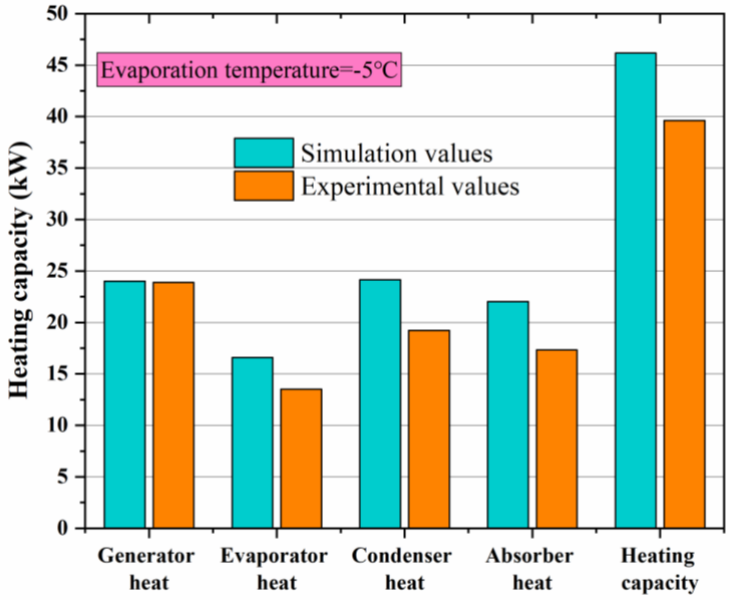

(a)

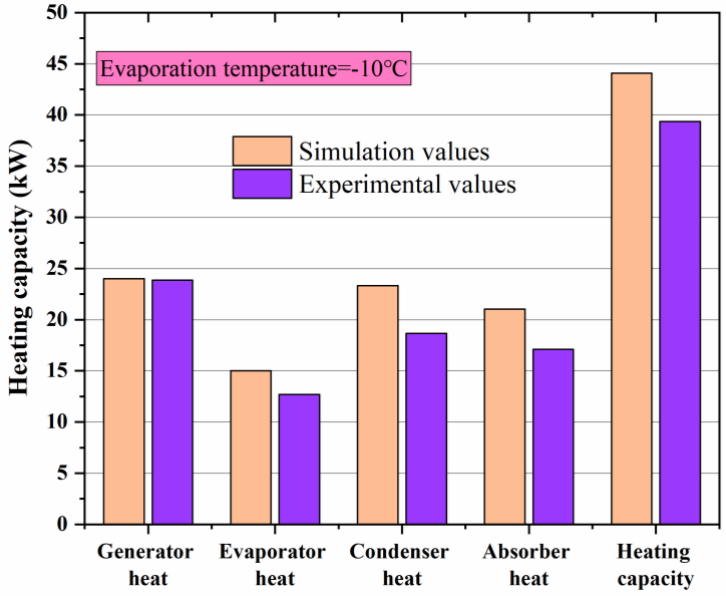

(b)

Fig. 8 Heat load of each components under experiment and simulation value

Fig. 9 symbolizes the variety of supply water temperature and COP with the increase of water flow rate under different evaporation temperatures. From Fig. 9, the COP rises while the supply water temperature declines with the growing water flow rate. Fig. 9(a) indicates that when the water flow rate is 1.52 m^3/h, the supply water temperature is 39.1 ℃ and the COP is 1.39; while the supply water temperature is 31.1 ℃ and the COP is 1.61 at the water flow rate of 2.4 m^3/h. According to the Fig. 9(b), when the water flow rate is 1.53 m^3/h, the supply water temperature is 38.9 ℃ and the COP is 1.38; while the supply water temperature is 31.2 ℃ and the COP is 1.53 at the water flow rate of 2.41 m^3/h. This is because that a higher water flow rate leads to the decrease of condensing temperature which will lead to the decrease of working fluid enthalpy in the condenser outlet. This will increase the heat load of the condenser, leading to progressed heating capacity and COP.

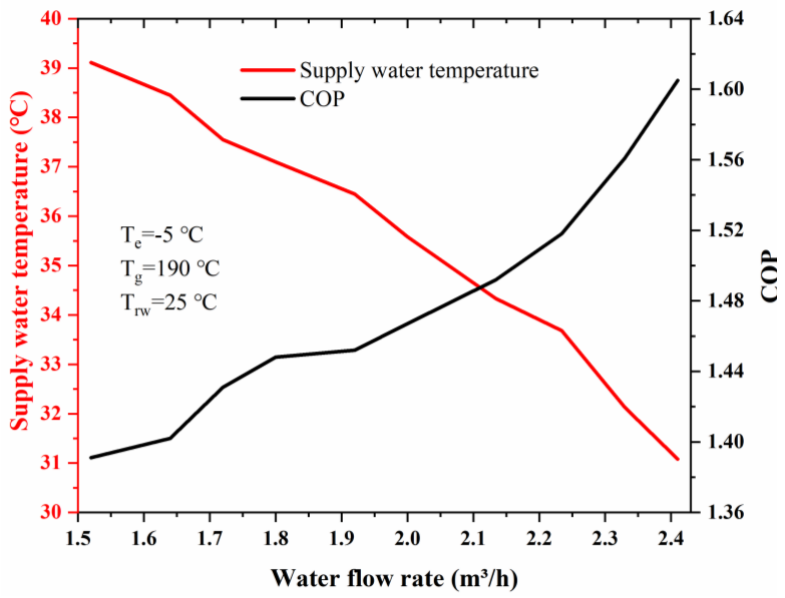

(a)

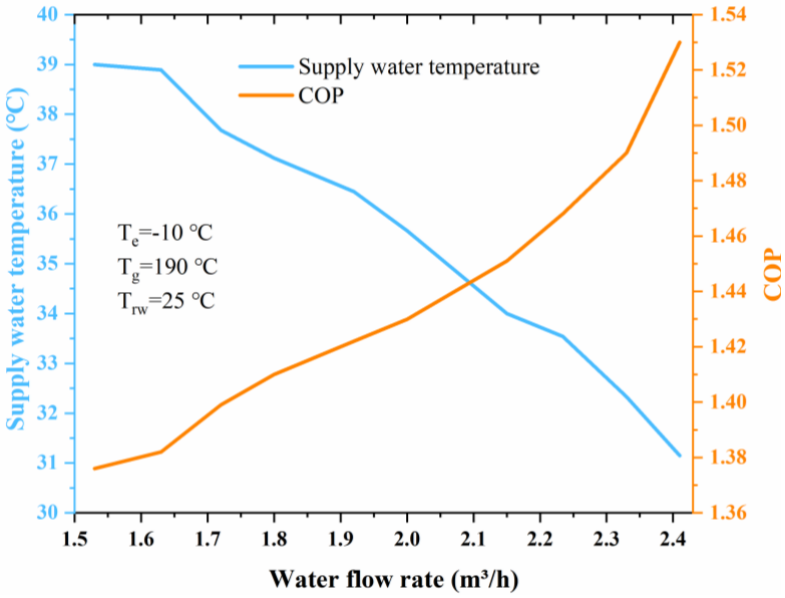

(b)

Fig. 9 Variation of supply water temperature and COP with the increase of water flow rate

4.2. System optimization

It can be seen from Fig. 9 that there is a conflict between the COP and water supply temperature with the increase of the water flow rate. Under different

evaporation temperatures, a higher COP leads to a lower water supply temperature while a higher water supply temperature results in a lower COP. Multi-objective optimization of the ASAHP system introduced in Section 3.2 has been conducted based on the TOPSIS decision-making and the NSGA-II technology. Table 6 shows some tuning parameters applied in the optimization process which also has been adopted by a similar absorption heat pump system in Ref. [27].

Table 6 Tuning Parameters in optimization [27]

Tuning parameters	Value
Population size	100
Maximum number of generations	400
Probability of crossover	0.75
Probability of mutation	0.9
Selection process	Tournament
Tournament size	2

Based on the Eqs. (14-18), normalized COP and normalized supply water temperature on the Pareto frontiers based on the NSGA-II technology have been exhibited in Fig. 10. Normalized COP and normalized supply water temperature has been calculated according to the Eqs. (14) and (15). From Fig. 10, the ideal point can be achieved when the normalized COP and normalized supply water temperature are 1; the COP and supply water temperature will be maximum at this condition. While

the non-ideal point will be found when the normalized COP and normalized supply water temperature are 0; the COP and supply water temperature will be minimum at this condition. However, there is no ideal and non-ideal point in practice. When the normalized COP is 0 and normalized supply water temperature is 1, the system can be a supply water temperature based optimal design; while the normalized COP is 1 and the normalized supply water temperature is 0, the system will be a COP-based optimal design. Therefore, the TOPSIS decision-making method is applied to search for the optimal result on the Pareto frontier.

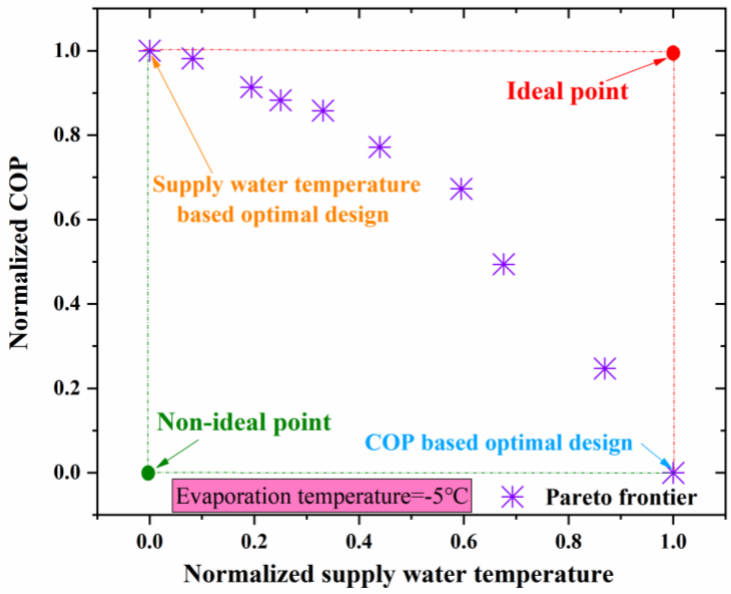

(a)

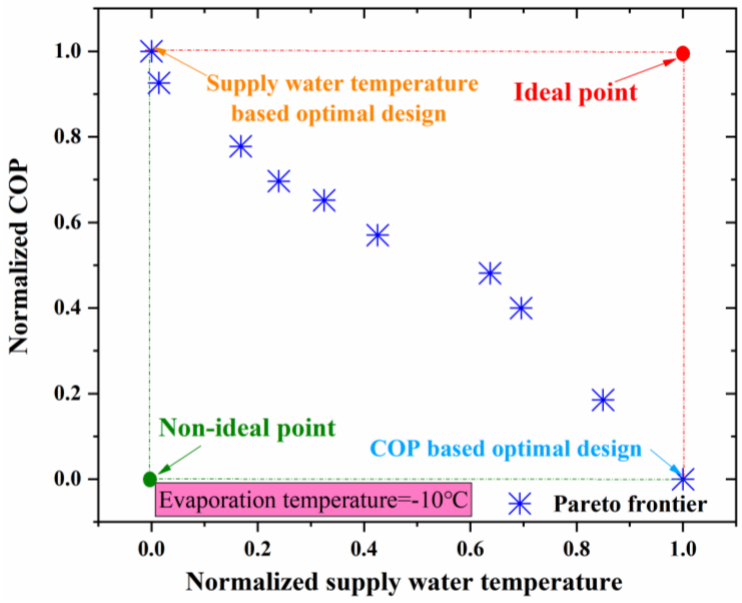

(b)

Fig. 10 Pareto frontier in optimization

Based on the Eqs. (16-18), the distance of any points to the ideal points d_{i+}, non-ideal points d_{i-} and proximity index Cl_i can be calculated. A maximum Cl_i will be elected as the optimal solution of the system. Fig. 11 shows the variation of d_{i+}, d_{i-} and Cl_i with normalized supply water temperature. It is shown that d_{i+} and d_{i-} firstly reduce and then rise with the increase of normalized supply water temperature; while the Cl_i firstly increases and then decreases. When the evaporation temperature is -5 ℃, the maximum Cl_i is 0.633 at the normalized supply water temperature of 0.595. In this condition, the supply water temperature is 34.3 ℃ and the COP is 1.49. When the evaporation temperature is -10 ℃, the maximum Cl_i is 0.558 at the normalized supply water temperature of 0.637. In this condition, the supply water temperature is 34.3 ℃ and the COP is 1.45. From Fig. 11, any points on the left-hand side of the MOP design line have better COP

performance; while those points on the right-hand side have better supply water temperature.

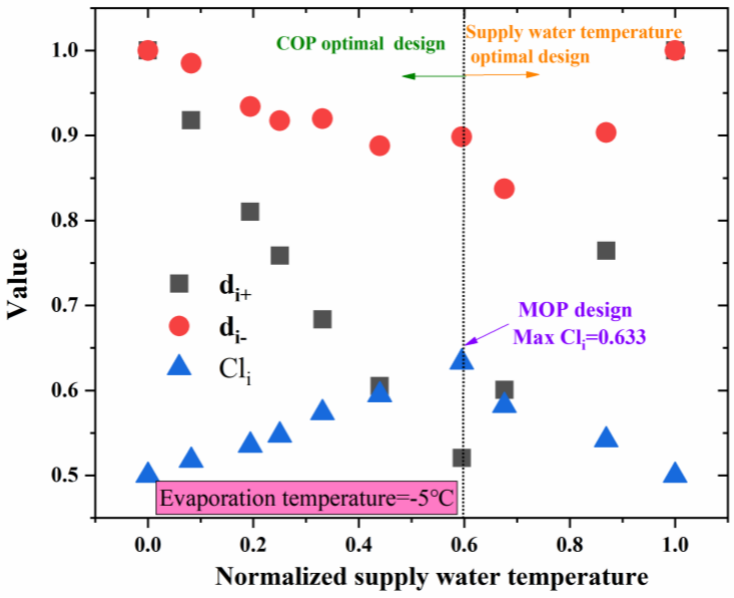

(a)

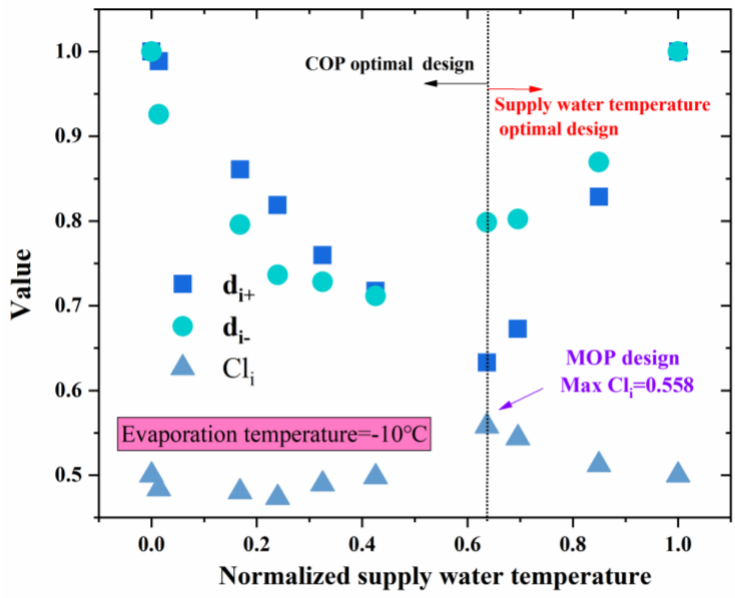

(b)

Fig. 11 The values calculated by the TOPSIS method

Table 7 indicates the COP, normalized COP, supply water temperature, and normalized supply water temperature in three optimization procedures. It can be seen that if COP-based optimized design is chosen as the final solution, the system can not inadequately meet supply water temperature design, and vice versa. If the COP-based optimized design is selected as the final solution, the average supply water temperature is 20.51 % lower than its maximum possible solution; whereas, if the supply water temperature-based optimized design is selected, the average COP is 10.97 % lower than its maximum possible solution. If the multi-objective optimization design is adopted, the average supply water temperature and COP will be 14.12 % and 5.22 % lower than their maximum values, respectively. Finally, the multi-objective optimization solutions are recommended as the optimal operating conditions, and the operating parameters are listed in Table 8.

Under the optimal operating conditions, the multi-objective optimization COPs are 1.49 at the evaporation temperature of -5 ℃ and 1.45 at the evaporation temperature of -10 ℃. The multi-objective optimization supply water temperatures are 34.3 ℃ at the evaporation temperature of -5 ℃ and 34.1 ℃ at the evaporation temperature of -10 ℃. According to Ref. [21], the author introduced an air-source absorption heat pump for heating. When the evaporation temperature was 0 ℃, the system could provide 30 kW heating capacity and the water was heated from 34.2 ℃ to 55.1 ℃ with the COP of 1.66. When evaporation temperatures are reduced to -5 ℃ and -10 ℃, the COP at the evaporation temperature of -5 ℃ and COP at the evaporation temperature of -10 ℃ are 1.51 and 1.40, respectively. It can be seen that

the COP in this study is lower than the COP in Ref. [21] at the evaporation temperature of -5 ℃; while COP in this study is higher than the COP in Ref. [21] at the evaporation temperature of -10 ℃. There are two reasons for the above results, which are different condensation temperatures and flue gas waste heat recovery in this study. The COP in this study is higher than that of the reference due to low condensation temperature, while the COP in this study is lower than that of the reference due to no flue gas waste heat recovery. However, the COPs of this study and reference are similar which indicates the feasibility of the ASAHP.

4.3. CO_2 emission estimation

With the growing attention about global warming and environmental problems, the system emission of CO_2 should be considered. Taking the typical working condition as an example, the gas consumption of the system is 2.42 m^3/h and the heating capacity is 39.34 kW. According to Ref. [41], CO_2 emission produced in the combustion can be calculated by this equation ($CH_4+2[O_2+3.76N_2]\rightarrow CO_2+2H_2O+7.52N_2$). The CO_2 produced per cubic meter of natural gas is 2.16 kg/m^3, the CO_2 produced per kilogram of coal is 1.9 kg/kg and the CO_2 emission factor of electricity is 0.88 kg/kWh [42]. When the annual operation time for heating is assumed to be 3600 h, the annual carbon dioxide emission is 31.49 t. Under the same heating capacity of 39.34 kW, the CO_2 emission of the coal is 46.33 t.

Table 7 Supply water temperature and COP value under three optimization procedure

Optimization parameters	Supply water temperature (℃)		COP		Normalized supply water temperature		Normalized COP	
Evaporating temperature (℃)	-5	-10	-5	-10	-5	-10	-5	-10
COP optimal design	31.1	31.2	1.61	1.53	0	0	1	1
Supply water temperature optimal design	39.1	38.9	1.39	1.38	1	1	0	0
Multi-objective optimization design	34.3	34.1	1.49	1.45	0.595	0.637	0.673	0.481

Table 8 The optimal operating conditions under different evaporation temperature

Parameters	T_{evap}=-5 ℃	T_{evap}=-10 ℃
Q_{evap} (kW)	16.81	16.23
Q_{cond} (kW)	28.35	28.15
Q_{gen} (kW)	23.69	23.87
Q_{abs} (kW)	13.66	11.98
COP	1.49	1.45
Heating capacity (kW)	40.35	39.45

5. Conclusions

A novel air-source absorption heat pump system (ASAHP) for heating is presented and designed. Fundamental of the system has been described firstly and a mathematical model based on the first law of thermodynamic is established. Then an experiment rig of the ASAHP driven by natural gas is built to examine the system performance. A typical operating condition is conducted to analyze the heat load and COP. Moreover, influences of the various generator temperature, condensing temperature, evaporation temperature, and water flow rate are investigated and analyzed. Finally, a multi-objective optimization is carried out to find the optimal operating condition for the system based on the TOPSIS and NSGA-II technology. According to the experiment analysis, the following conclusions are listed:

1. The proposed system has good stability and feasibility at the different operational conditions, and can absorb heat from the outdoor air and provide heating efficiently.
2. The increase in generator temperature has a positive effect on COP and heating capacity. When the evaporation temperature is -10 ℃, the system can achieve a maximum 38.32 kW heating capacity and 41.32 kW heating capacity$_{fg}$ with a COP of 1.39 and COP$_{fg}$ of 1.53 at the generator temperature of 190 ℃. The maximum ratio of COP$_{fg}$ to simulation value is about 92.91 % and the maximum ratio of heating capacity$_{fg}$ to simulation value is about 92.23 %.
3. The increase in supply water temperature harms COP and heating capacity.

Under the different working conditions, the system can achieve an average 36.2 kW heating capacity to heat water from 25 ℃ to 39.1 ℃ with an average COP of 1.23 and an average COP_{fg} of 1.36. If the water is heated from 25 ℃ to 30.7 ℃, the average COP increases from 1.23 to 1.56. The maximum ratio of COP_{fg} to simulation value is about 93.67 % and the maximum ratio of heating $capacity_{fg}$ to simulation value is about 91.33 %.

4. A lower supply water temperature may cause a higher COP and vice versa. Both designs are not optimal but multi-objective optimization can solve the conflict problem. If the multi-objective optimization design is selected, the average supply water temperature and the average COP are 14.12 % and 5.22% lower than their maximum possible values, respectively.

Acknowledgement

This work was supported by the Natural Science Foundation of Tianjin (No. 19JCQNJC07200) and National Key R&D Program of China (No. 2018YFC0705000)

Appendix A

Table A1 Coefficients in Eqs.(1-3)

n	A_n	B_n	C_n	$A_n^{c_p}$	$B_n^{c_p}$	$C_n^{c_p}$	G_n
0	5.21E+01	-5.58E+03	-6.34E+00	2.79E+02	-4.2E-02	2.31E-03	-1.90E+04
1	1.27E+01	3.39E+03	-1.43E+00	-1.51E+02	5.98E-01	-5.97E-03	8.72E+03
2	-1.39E+02	-8.60E+03	2.23E+01	1.01E+02	-1.37E+00	3.43E-03	-1.39E+03
3	7.32E+02	-3.16E+03	-1.14E+02	-1.28E+02	1.02E+00	1.05E-03	-6.42E+02
4	-1.19E+03	3.04E+04	1.81E+02	-	-	-	-
5	5.47E+02	-1.90E+04	-8.19E+01	-	-	-	-

References

[1] Yang L, Yan H, Lam JC. Thermal comfort and building energy consumption implications-a review. Applied Energy 2014; 115:164-73.

[2] Tsinghua University Building Energy Saving Research Center. Annual Report on China Building Energy Efficiency. Beijing: China Architecture and Building Press; 2017. [in Chinese].

[3] Wu ZX, Zhang YF, He ZL et al. Performance investigation of a bi-functional integration system for power and heat supply. Applied thermal engineering 2019; 148:714-721.

[4] Halit A, Oguz A. Exergoeconomic analysis of district heating system boosted by the geothermal heat pump. Energy 2017;119: 1159-1170.

[5] Mahdi De, Sajjad V, Ahmad A. Simultaneous use of air-side and water-side economizers with the air source heat pump in a data center for cooling and heating production. Applied thermal engineering 2019;161:114113.

[6] Yu M, Li S, Zhang XJ et al. Techno-economic analysis of air source heat pump combined with latent thermal energy storage applied for space heating in China. Applied Thermal Engineering 2021;185:116434.

[7] Long JB, Xia KM, Zhong HH et al. Study on energy-saving operation of a combined heating system of solar hot water and air source heat pump. Energy Conversion and Management 2021;229:113624.

[8] Wu P, Wang ZC, Li XF et al. Energy-saving analysis of air source heat pump

integrated with a water storage tank for heating applications. Building and Environment 2020;180:107029.

[9] Lu D, Chen GF, Gong MQ et al. Thermodynamic and economic analysis of a gas-fired absorption heat pump for district heating with cascade recovery of flue gas waste heat. Energy Conversion and Management 2019;185:87-100.

[10] Wu W, You T, Wang BL et al. Simulation of a combined heating, cooling and domestic hot water system based on ground source absorption heat pump. Applied Energy 2014;126: 113-122.

[11] Zhang QL, Cao MK, Zhang QY et al. Research on a New District Heating Method Combined with Hot Water Driven Ground Source Absorption Heat Pump. Energy Procedia 2015;75:1242-1248.

[12] Anna N, Robert S. Comparison of LCA results of low temperature heat plant using electric heat pump, absorption heat pump and gas-fired boiler. Energy Conversion and Management 2014;87:647-652.

[13] Christopher M. K, Srinivas G, Michael A. G. Modeling of an ammonia–water absorption heat pump water heater for residential applications. International Journal of Refrigerant 2017; 83:39-50.

[14] Wu W, Wang BL, You T et al. Configurations of solar air source absorption heat pump and comparisons with conventional solar heating. Applied thermal engineering 2018;141: 630-641.

[15] Garrabrant M, Stout R, Glanville P, et al. Development and validation of a gas-fired residential heat pump water heater-final report. Stone Mountain

Technologies, Inc 2013.

[16] Altamash A B, Kajen E, Alan F. Development of a Monitoring System for a Gas-Fired Absorption Heat Pump and Results for Testing in Heating and Cooling Mode. Energy Procedia 2019; 158:2202-2209.

[17] Dai EQ, Jia T, Dai YJ. Theoretical and experimental investigation on a GAX-Based NH_3-H_2O absorption heat pump driven by parabolic trough solar collector. Solar energy 2020;197:498-510.

[18] Garimella S, Christensen RN, Lacy D. Performance evaluation of a generator-absorber heat-exchange heat pump. Applied Thermal Engineering 1996;16(7):591-604.

[19] Fukuta M, Yanagisawa T, Iwata H et al. Performance of compression/absorption hybrid refrigeration cycle with propane/mineral oil combination. International Journal of Refrigerant 2002;25(7):907-15.

[20] Wu W, Wang B, Shang S, et al. Experimental investigation on NH_3-H_2O compression-assisted absorption heat pump (CAHP) for low temperature heating in colder conditions. International Journal of Refrigerant 2016;67:109-24.

[21] Lu D, Bai Y, Zhao YX et al. Experimental investigations of an absorption heat pump prototype with intermediate process for residential district heating. Energy Conversion and Management 2020;204:112323.

[22] Shang S, Li X, Chen W, et al. A total heat recovery system between the flue gas and oxidizing air of a gas-fired boiler using a non-contact total heat exchanger.

Applied Energy 2017;207:613-23.

[23] Qu M, Omar A, Yin HX. New configurations of a heat recovery absorption heat pump integrated with a natural gas boiler for boiler efficiency improvement. Energy Conversion and Management 2014;87: 175-184.

[24] Yang B, Jiang Y, Fu L et al. Experimental and theoretical investigation of a novel full-open absorption heat pump applied to district heating by recovering waste heat of flue gas. Energy Build 2018;173:45-5.

[25] Robabeh. A.H, Scott J.O. An elliptic numerical analysis of water vapour absorption into a falling film in vertical parallel plate channels. International Journal of Heat and Mass Transfer 2020;150: 119266.

[26] Hu B, Yan HZ, Wang RZ. Modeling and simulation of a falling film evaporator for a water vapor heat pump system. Applied Energy 2019;255:113851.

[27] Jain V, Sachdeva G. Energy, exergy, economic (3E) analyzes and multi-objective optimization of vapor absorption heat transformer using NSGA-II technique. Energy Conversion and Management 2017;148: 1096-1113.

[28] Wu ZX, You SJ, Zhang H et al. Performance analysis and optimization for a novel air-source absorption heat pump. Energy Conversion and Management 2020; 233:113423.

[29] Yuan H, Zhang J, Huang XK et el. Experimental investigation on binary ammonia-water and ternary ammonia-water-lithium bromide mixture-based absorption refrigeration systems for fishing ships. Energy Conversion and Management 2018;166:13-22.

[30] Nico M, Fabian S, Bernd B et al. Design and analysis of an ammonia-water absorption heat pump. Applied Thermal Engineering 2020;165:114531.

[31] Ando E, Takcshito I. Residential gas-fired absorption heat pump based on R22-DEGDME Pair, Part 1: thermodynamic properties of R22-DEGDME Pair. International Journal of Refrigeration 1984; 7: 181-185.

[32] Takcshito I, Yamamoto Y, Harada T et al. Residential gas-fired absorption heat pump based on R22-DEGDME Pair, Part 2: design, computer simulation and testing of a prototype. International Journal of Refrigeration 1984; 7: 313-321.

[33] Wu ZX, Sha L, Zhao MZ et al. Performance analyzes and optimization of a reverse Carnot cycle-organic Rankine cycle dual-function system. Energy Conversion and Management 2020;212:112787.

[34] Deb K, Pratap A, Agarwal S, Meyarivan T. A fast and elitist multi-objective genetic algorithm: NSGA-II. IEEE Transactions Evolutionary Computation 2002;6:182–197.

[35] Wang YZ, Zhao J, Wang Y et al. Multi-objective optimization and grey relational analysis on configurations of organic Rankine cycle. Applied Thermal Engineering 2017;114: 1355-1363.

[36] Rasikh T, Ali S, J. X et al. Multi-objective optimization for the best possible thermal, electrical and overall energy performance of a novel perforated-type regenerative evaporative humidifier. Energy Conversion and Management 2019;198:111802.

[37] Wu ZX, Zhang YF, Sheng Y. Energy, exergy, economic(3E) analysis and

multi-objective optimization of a novel dual functional integration system. Energy Conversion and Management 2019;199:111962

[38] Yao S, Zhang YF, Yu XH. Thermo-economic analysis of a novel power generation system integrating a natural gas expansion plant with a geothermal ORC in Tianjin, China. Energy 2018; 164: 602-614.

[39] Wu ZX, Sha L, Yang XC et al. Performance evaluation and working fluid selection of combined heat pump and power generation system (HP-PGs) using multi-objective optimization. Energy Conversion and Management 2020;221:113164.

[40] Wu ZX, Wang YR, You SJ et al. Thermo-economic analysis of composite district heating substation with absorption heat pump. Applied thermal engineering 2020;166:114659.

[41] Rasikh T, Nadeem A, J. X et al. An innovative air saturator for humidification-dehumidification desalination application. Applied Energy 2018;228:789-807.

[42] Rasikh T, J. X, A. B et al. Multidimensional assessment of a photovoltaic air collector integrated phase changing material considering Mexican climatic conditions. Energy 2020; 209:118304.